batteries

MDPI

Article

Surface Modification Induces Oriented Zn(002) Deposition for Highly Stable Zinc Anode

Hongfei Zhang, Fujie Li, Zijin Li, Liu Gao, Binghui Xu * and Chao Wang *

Institute of Materials for Energy and Environment, College of Materials Science and Engineering, Qingdao University, Qingdao 266071, China

* Correspondence: xubinghuiqdu@qdu.edu.cn (B.X.); wangc@qdu.edu.cn (C.W.)

Abstract: Aqueous zinc metal batteries (AZMBs) are considered a promising candidate for grid-scale energy storage systems owing to their high capacity, high safety and low cost. However, Zn anodes suffer from notorious dendrite growth and undesirable surface corrosion, severely hindering the commercialization of AZMBs. Herein, a strategy for engineering a dense ZnO coating layer on Zn anodes using the atomic layer deposition (ALD) technique is developed, aiming to improve its long-term cycling stability with fewer Zn dendrites. The surface-modified Zn anode (ZnO@Zn) exhibits an excellent long-cycling life (680 h) and stable coulombic efficiency when being used in a symmetric cell. Moreover, the ZnO@Zn electrode shows a high stability with almost no capacity decay after 1100 cycles at 2C in a full cell using MnO_2 as the cathode. The ZnO coating is conducive to reducing corrosion and the generation of by-products, thus increasing the reversibility of Zn^{2+}/Zn stripping/plating. Particularly, density functional theory (DFT) calculation results reveal that the ZnO coating layer could effectively lower the adsorption energy of the Zn(002) plane in ZnO@Zn, inducing the preferential deposition of Zn^{2+} towards the (002) crystal plane with fewer Zn dendrites. The surface ZnO coating protocol provides a promising approach to achieve a dendrite-free Zn anode for stable AZMBs.

Keywords: aqueous zinc metal batteries; surface coating; zinc dendrites; long-term stability

Citation: Zhang, H.; Li, F.; Li, Z.; Gao, L.; Xu, B.; Wang, C. Surface Modification Induces Oriented Zn(002) Deposition for Highly Stable Zinc Anode. *Batteries* **2024**, *10*, 178. https://doi.org/10.3390/batteries10060178

Academic Editors: Guanjie He, Haobo Dong and Jie Lin

Received: 30 April 2024
Revised: 20 May 2024
Accepted: 22 May 2024
Published: 24 May 2024

1. Introduction

Rechargeable AZMBs have emerged as one of the best choices for grid-scale energy storage systems owing to the appealing merits of high theoretical capacity (820 mAh g^{-1} or 5855 mAh cm^{-3}), low redox potential (−0.762 V vs. SHE), high safety, low cost and environmental friendliness [1–3]. However, Zn anodes suffer from poor cycling stability due to the notorious dendrite growth, undesirable surface passivation and hydrogen evolution reaction (HER), greatly hindering the commercial application of AZMBs [4,5]. Uncontrolled Zn dendrites during cycling inevitably increase the contact area with electrolyte, leading to the acceleration of hydrogen corrosion [6,7]. The concomitant HER promotes the formation of parasitic Zn^{2+} insulating byproducts and in turn boosts uneven Zn deposition, inducing low redox kinetics and poor cycling stability [3]. Therefore, it is urgently needed to construct rational interfaces between Zn and electrolyte for highly reversible AZMBs.

Strategies have been demonstrated to address the problems of Zn anodes, including surface modification [8,9], electrolyte optimization [10,11] and structural construction [6,12]. The construction of artificial interface layers such as metal–organic frameworks [13], covalent organic frameworks [14], oxide materials [15], carbon-based materials [16], etc., has been shown to be an effective strategy for suppressing the growth of Zn dendrites. In general, coated layers can effectively reduce the contact of electrode and electrolyte, and minimize the occurrence of HERs [1]. For instance, a surface-modified Zn anode maintained a high-capacity retention of 88.9% after 600 cycles owing to the coating of a metal–organic framework layer, which can help the formation of a super-saturated front surface with low interface resistance [14].

Constructing a laponite nano-clay layer on the Zn anode improves its long-term cycling stability due to the existence of negative and positive electric fields together, thus inducing Zn^{2+} nucleation for preferential orientation growth with fewer Zn dendrites [17]. Among various materials, zinc dioxide (ZnO) coating has been widely reported in the surface modification research owing to its excellent chemical stability and stable corrosion resistance [15,18–21]. For example, Chen et al. prepared vertically aligned ZnO hexagonal columns onto Zn foil via a chemical solution method, which promoted homogenous and nearly horizontal Zn plating [18]. Peng et al. reported that ZnO nanowire arrays growing on Zn foil by a horizontally potentiostatic anodizing technique could provide uniform nucleation sites and high electrical conductivity for the Zn metal anode, which was beneficial for improved cyclic performance [15]. Nevertheless, the abovementioned surface modification strategies for ZnO layers contain complex chemical or electrochemical procedures, which inhibit their practical application. What is more, the thickness of coated ZnO cannot be precisely controlled using the abovementioned methods, which is crucial to charge transports for AZMBs. Therefore, it is necessary to develop a simple and controllable coating strategy for ZnO layers on Zn anodes for large-scale application.

As Zn^{2+}/Zn stripping/plating is highly associated with the surface atomic structure, intensive attention has been paid to constructing special crystal planes for Zn anodes [9,16,22–24]. In general, the (002) crystal plane exhibits a lower surface energy than that of other crystal planes of Zn anodes, resulting in low electrochemical activity of HERs [25]. Moreover, the (002) surface possesses an even interfacial charge density, which is helpful for uniform Zn^{2+}/Zn plating, thus reducing Zn dendrites [26]. For example, Ma and coworkers proposed a sodium hyaluronate (SH) coating strategy to regulate the charge distribution on the Zn surface, which induced the preferential deposition of Zn towards the (002) crystal plane [27]. The modified Zn anode exhibited an impressive long-term cycling stability with 6300 h Zn^{2+}/Zn stripping/plating. A surface-modified Zn anode presented long cycling stability owing to the coating of a $AgZn_3$ coating layer [9], which can help the ordered Zn(002) epitaxial deposition with dendrite-free Zn growth. Overall, the key to surface modification for Zn anodes is the construction of a desirable surface texture, which can help it to achieve high reversibility of Zn^{2+}/Zn stripping/plating.

In this work, we succeeded in coating a dense ZnO layer on Zn anodes using the ALD technique, aiming to improve their long-term cycling stability with fewer Zn dendrites. The modified Zn anode (ZnO@Zn) with controllable thickness exhibits an impressive long-cycling life (680 h) and stable coulombic efficiency when being used in a symmetric cell at a current density of 1 mA cm^{-2}. Moreover, the ZnO@Zn electrode shows high stability with almost no capacity decay after 1100 cycles at 2C in a full cell using MnO_2 as the cathode. The ZnO coating is conducive to reducing corrosion and the generation of by-products, thus increasing the reversibility of Zn^{2+}/Zn stripping/plating. What is more, the ZnO layer can effectively lower the adsorption energy of the Zn(002) plane in ZnO@Zn, inducing the preferential deposition of Zn towards the (002) crystal plane with fewer Zn dendrites. This oxide coating modification provides a promising strategy to achieve dendrite-free Zn anodes for stable AZMBs.

2. Materials and Methods

Materials. All chemicals, including Zn foil (Aladdin Biochemical Technology Co., Ltd., Shanghai, China), diethyl zinc (Sigma-Aldrich (Shanghai) Trading Co., Ltd., Shanghai, China), H_2SO_4 (95%~98%, Sinopharm Chemical Reagent Co., Ltd., Shanghai, China), $MnSO_4 \cdot H_2O$ (Aladdin), $KMnO_4$ (Sinopharm Chemical Reagent Co., Ltd., Shanghai, China), $ZnSO_4$ (Aladdin Biochemical Technology Co., Ltd., Shanghai, China), N-methyl pyrrolidone (NMP, Aladdin Biochemical Technology Co., Ltd., Shanghai, China), polyvinylidene fluoride (PVDF, Solvay (Shanghai) Co., Ltd., Shanghai, China) and Super P (Timcal Super C65), were used as received.

Preparation of ZnO@Zn. The ZnO layer was coated on Zn foil using the ALD (MNT-S, Jiangsu MNT Micro and Nanotech Co., Ltd., Wuxi, China) technique with diethyl zinc as the Zn source and H_2O as the oxygen source. Typically, a piece of Zn foil was loaded in the

ALD reaction chamber. After the reactor temperature reached 170 °C, the ALD cycle started with vapors of precursors pulsing in the chamber as follows: (1) diethyl zinc for 0.5 s; (2) N_2 for 40 s; (3) H_2O for 0.1 s; (4) N_2 for 40 s. The coated samples obtained after 30, 50 and 70 ALD cycles were denoted as ZnO@Zn-30, ZnO@Zn and ZnO@Zn-70, respectively.

Preparation of MnO_2. A total of 2 mL 0.5 M H_2SO_4 and 0.507 g $MnSO_4 \cdot H_2O$ were dissolved in 50 mL distilled water and magnetically stirred for 10 min. Then, 20 mL 0.1 M $KMnO_4$ was slowly added to the above solution. The mixture was stirred for 30 min, followed by transfer to a Teflon-lined stainless-steel autoclave. The autoclave was maintained at 120 °C for 24 h. After cooling to room temperature, the product was centrifuged, washed repeatedly using deionized water and dried overnight at 60 °C.

Materials Characterizations. The phase and crystal structures of the samples were characterized on an Ultima IV powder X-ray diffractometer (Rigaku Co., Ltd., Tokyo, Japan) with Cu Kα radiation (λ = 1.5406 Å) at a scanning speed of 10° min^{-1}. Morphologies and compositions of the samples were characterized by using field-emission scanning electron microcopy (FESEM, JSM-7800F, JEOL (Beijing) Co., Ltd., Beijing, China) equipped with an energy dispersive function at an accelerating voltage of 10 kV. Surface analysis was performed using X-ray photoelectron spectroscopy (XPS, PHI5000 Ver-saprobe III) with an X-ray source of Al Kα.

Electrochemical Measurements. The Tafel curves and linear sweep voltammetry (LSV) were collected by an electrochemical workstation (CHI 660E, Shanghai Chenhua Instrument Co., Ltd., Shanghai, China) using a standard three-electrode system with Zn or ZnO@Zn as working electrode, Pt as counter electrode and $Ag/AgCl_2$ as reference electrode. The coin cells (CR-2032, Shenzhen Neware Electronics Co., Ltd., Shenzhen, China) were adopted to analyze the electrochemical performance and the half cells, symmetric cells and full cells used in this experiment were assembled in air atmosphere using glass fibers as separators. A 2M $ZnSO_4$ was used as the electrolyte in the three-electrode system, half cells and symmetric cells. A half cell was assembled using ZnO@Zn or Zn as the working electrodes and Cu as counter electrode. The symmetrical cell was assembled using Zn or ZnO@Zn as both the working and counter electrodes. The full cell was assembled using ZnO@Zn or Zn as the anode and MnO_2 as the cathode with a 2M $ZnSO_4$ + 0.1M $MnSO_4$ aqueous solution as the electrolyte. The MnO_2 electrodes were prepared with MnO_2, Super P and PVDF in a mass ratio of 80:10:10. These electrode ingredients were dispersed in NMP. The obtained slurry was painted on the aluminum foil and dried in a vacuum oven at 110 °C for 12 h. The loading of the active material was 1.3–1.5 mg cm^{-2}. Charge–discharge measurements were performed using a Neware instrument (CT-4008, Shenzhen Neware Electronics Co., Ltd., Shenzhen, China) over a voltage range of 0.8 to 1.8 V. The measurements of long-term cycling performance were performed using the cells after the tests of rate performance. Cyclic voltammetry (CV) was collected using the Bio-Logic electrochemical workstation (SP-150, Bio-Logic Co., Ltd., Seyssinet-Pariset, France) at different scan rates over a voltage range of 0.8 to 1.8 V. The electrochemical workstation was also used to measure for electrochemical impedance spectroscopy (EIS) with an AC stimulus of 10 mV and amplitude frequencies in the range of 100 kHz to 0.01 Hz.

Theoretical Computation. Structural optimization was performed using the Vienna Ab-initio Simulation Package (VASP) with the projector augmented wave (PAW) method [28,29]. The exchange functional was treated using the Perdew–Burke–Ernzerhof (PBE) functional to describe the weak interactions between atoms. The cut-off energy of the plane wave basis was set at 500 eV in structural optimization. For the optimization of both geometry and lattice size, the Brillouin zone integration was performed with a Gamma point. Partial occupancies of the Kohn–Sham orbitals were allowed using the Gaussian smearing method and a width of 0.05 eV. A geometry optimization was considered convergent when the energy change was smaller than 0.02 eV $Å^{-1}$. To consider the strong correlation effects of transition metal in structure, both structural optimizations and electronic structure calculations were carried out by using the spin-dependent GGA plus Hubbard correction U method. Vacuum slab models were used to calculate the adsorption of ZnO atoms on

Zn(002) and (101) surfaces. These Zn surface slabs comprised four layers of Zn atoms, and a vacuum region of 20 Å above them was used to ensure decoupling between neighboring systems. The top two layers were allowed to relax while the bottom two layers were fixed fully.

The surface free energy (γ) was calculated using this expression based on a previous study [30]:

$$\gamma = \frac{E^{slab} - E_{Zn}^{bulk} - E_{ZnO}^{bulk}}{2A}$$

where Eslab is the total energy of the slab, Ebulk Zn is the energy of Zn model, Ebulk ZnO is the energy of ZnO model and A is the area of the model surface.

3. Results and Discussion

Figure 1 schematically illustrates the preparation procedure for ZnO@Zn and its Zn-plating behaviors. A ZnO layer can effectively reduce the contact of a Zn anode and the electrolyte, thus minimizing the occurrence of HERs and inhabiting side reactions [18]. This helps ZnO@Zn to achieve high reversibility of Zn^{2+}/Zn stripping/plating during cycling with fewer Zn dendrites.

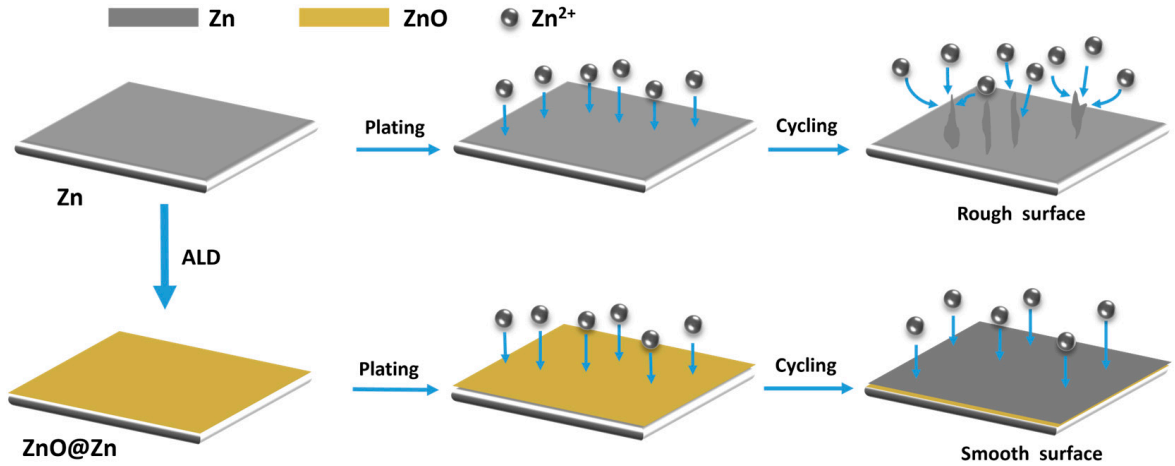

Figure 1. Schematic illustration of preparation procedure for ZnO@Zn and the plating behaviors of bare Zn and ZnO@Zn electrodes.

Figure 2a compares the XRD patterns of bare Zn and ZnO@Zn. All the diffraction peaks of ZnO@Zn are in agreement with the standard card (Power Diffraction File No. 04-0831) without any impurities after coating ZnO [27]. The ZnO@Zn exhibits a higher intensity ratio of $I_{(002)}/I_{(101)}$ (0.72) than that of bare Zn (0.45), demonstrating the enhanced (002) texture. This is beneficial for the parallel deposition of Zn^{2+} to the surface direction, thus lessening the amount of Zn dendrites [23]. Figure 2b shows the high-resolution Zn2p XPS spectra of bare Zn and ZnO@Zn. There are two characteristic peaks at 1045.3 and 1022.2 eV for ZnO@Zn, corresponding to $Zn2p_{1/2}$ and $Zn2p_{3/2}$ [26,31]. The strong electronic interaction between zinc metal and oxygen in ZnO@Zn causes a shift in Zn2p peak position towards lower energy [32], which can confirm the successful coating of a ZnO layer on the surface of bare Zn via ALD. Figure S1 compares the Raman spectra of bare Zn and ZnO@Zn. The sharp peak at about 100 cm^{-1} is ascribed to the characteristic peak of metallic zinc [15]. There is a new peak at about 560 cm^{-1} for ZnO@Zn, corresponding to the vibration of the Zn-O bond [18], which further confirms the successful coating of ZnO layer.

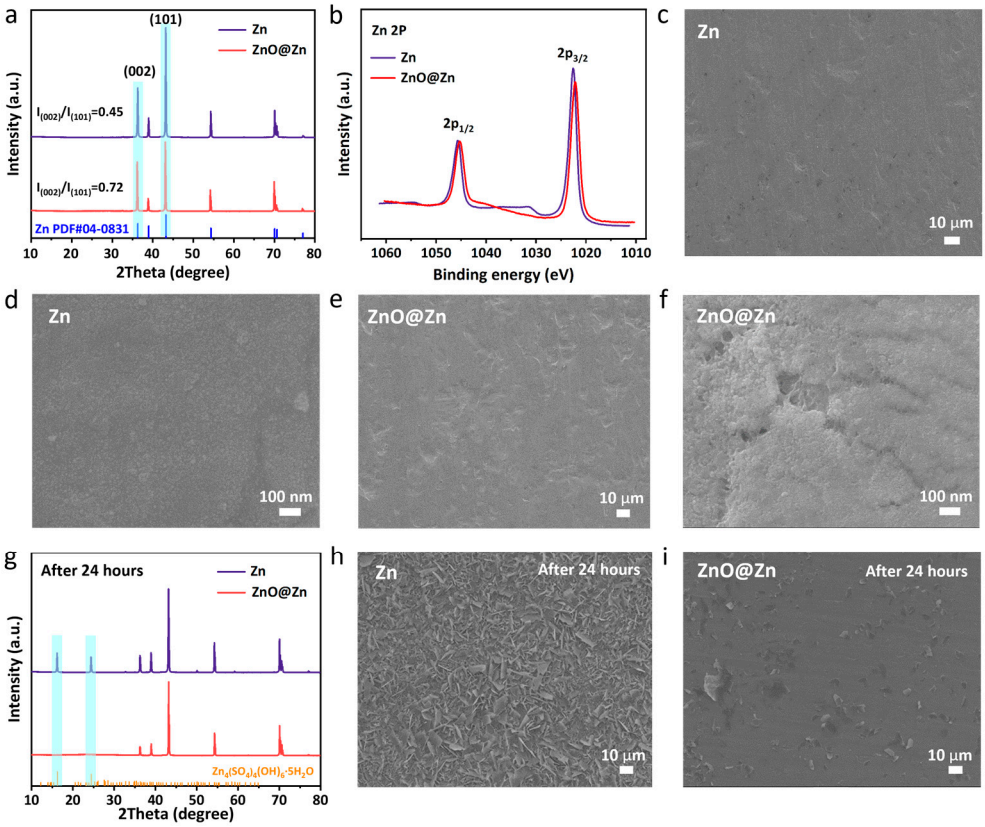

Figure 2. (**a**) XRD patterns of bare Zn and ZnO@Zn. (**b**) High-resolution Zn 2p XPS spectrum of bare Zn and ZnO@Zn. SEM images of bare Zn (**c**,**d**) and ZnO@Zn (**e**,**f**). (**g**) XRD patterns of bare Zn and ZnO@Zn; SEM images of bare Zn (**h**) and ZnO@Zn (**i**) after 24 h immersion.

Figure 2c,d and Figure 2e,f show the FESEM images of bare Zn and ZnO@Zn, respectively. After coating, ZnO@Zn exhibits a rough surface morphology with a dense textured ZnO layer on the surface, further confirming the successful deposition after ALD treatment. Figures S2 and S3 show the SEM images of ZnO@Zn-30 and ZnO@Zn-70, respectively. ZnO@Zn-30 exhibits a sparser morphology of ZnO layers and ZnO@Zn-70 shows larger spherical ZnO particles than those of ZnO@Zn. The cross-sectional FESEM images of ZnO@Zn are shown in Figure S4. It can be seen that the surface of ZnO@Zn has a coating layer with a thickness of about 10 nm. Figure S5 shows a high-resolution TEM image of ZnO, which is stripped from the surface of ZnO@Zn. The coating layer exhibits obvious crystal structure with an interplane spacing of 2.473 nm, corresponding to the (002) plane of ZnO [18].

To visually confirm the superior corrosion resistance of the ZnO@Zn, both bare Zn and ZnO@Zn were immersed in a highly concentrated $ZnSO_4$ solution (2 mol L^{-1}). Figure 2g compares the XRD patterns of bare Zn and ZnO@Zn after 24 h immersion. The bare Zn exhibits new peaks of $Zn_4SO_4(OH)_6{\cdot}5H_2O$ (ZSH, Power Diffraction File No. 39-0688) by-products [6], revealing its active interfacial reaction and corrosion on the surface. In contrast, the XRD patterns of the ZnO@Zn show no variation, confirming the positive effect of the ZnO layer in inhibiting ZSH generation. The corresponding SEM images after the immersion tests are shown in Figure 2h,i, where obvious dendrites and smooth morphology are observed on bare Zn and ZnO@Zn, respectively, which is consistent with the above XRD results. Overall, the ZnO coating is conducive to reducing corrosion and the generation of the ZSH by-products, thus increasing the reversibility of Zn^{2+}/Zn stripping/plating.

Figure 3a shows the Tafel curves of bare Zn and ZnO@Zn electrodes in the three-electrodes system. ZnO@Zn exhibits a higher hydrogen evolution overpotential than that of Zn, indicating the positive effect of a ZnO layer for corrosion inhibition [33,34]. Hydrogen evolution reactions (HERs) of bare Zn and ZnO@Zn were measured by linear

sweep voltammetry (LSV), and the results are shown in Figure 3b. Due to the ZnO coating, the ZnO@Zn electrode exhibits reduced current density of hydrogen reaction, which is beneficial for the inhibition of ZSH by-products [12]. Coulombic efficiency serves as a pivotal determinant in gauging battery lifespan and anode stability [35]. As shown in Figure 3c, the Zn||Cu half cell at 1 mA cm^{-2}/1 mAh cm^{-2} exhibits an abnormal coulombic efficiency after 300 cycles, which is ascribed to the short circuit caused by Zn dendrites. Conversely, for the ZnO@Zn||Cu cell with the same operating conditions, a near 100% coulombic efficiency was maintained after 1000 cycles, indicating a high reversibility of Zn^{2+}/Zn stripping/plating. Galvanostatic cycling curves of ZnO@Zn||Cu and Zn||Cu half cells are shown in Figures 3d and S6. The ZnO@Zn||Cu cell exhibits a lower average overpotential (15.2 mV) with better cycling repeatability than that of a Zn||Cu cell, further confirming the positive inhibition of HERs and enhanced reversibility of Zn^{2+} deposition due to the ZnO coating. Figure S7 shows a comparison of average voltage hysteresis in ZnO@Zn with that of the modified Zn anodes reported in the literature. Obviously, the ZnO@Zn in this work exhibits a lower voltage hysteresis than that of others, further demonstrating the positive effect of a ZnO coating layer on the excellent electrochemical performance of ZnO@Zn anodes.

Figure 3e compares the long cycling performance of Zn||Zn and ZnO@Zn||ZnO@Zn symmetric cells at 1 mA cm^{-2} with 1 mAh cm^{-2}. Compared with bare Zn, the ZnO@Zn||ZnO@Zn cell exhibits smaller voltage hysteresis. The Zn||Zn cell shows a sudden increase in voltage after 120 h cycling, which is ascribed to the short circuit caused by Zn dendrites [21]. In contrast, the ZnO@Zn||ZnO@Zn cell exhibits stable polarization voltage at 680 h with almost no apparent increase, demonstrating high reversibility of Zn^{2+}/Zn stripping/plating. Rate performance tests were conducted on both symmetric cells with bare Zn and ZnO@Zn electrodes, and the results are shown in Figure 3f. The ZnO@Zn symmetric cell shows more stable overpotentials at high current density than those of the Zn||Zn cell.

The growth behaviors of Zn dendrites on bare Zn and ZnO@Zn were observed by in situ optical microscopy, and the results are shown in Figure 3g,h. At a current density of 10 mA cm^{-2}, the bare Zn electrode started to form dendrites within 20 min and obvious protuberances emerged after 60 min depositing with a thickness of about 200 μm. Conversely, on the ZnO@Zn electrode, there were no obvious Zn dendrites on the surface. A thickness growth of about 50 μm could be observed due to the homogeneous plating of Zn^{2+}, demonstrating the positive effect of ZnO coating for the inhibition of dendritic growth [15].

To further illuminate the practical application of ZnO@Zn, several electrochemical tests were performed on full cells using MnO_2 as cathode and bare Zn or ZnO@Zn as anode in the voltage range of 0.8–1.8 V. The reactions occurring on the cathode and anode were $MnO_2 + 1/2Zn^{2+} + e^- = Zn_{1/2}MnO_2$ and $1/2Zn = 1/2Zn^{2+} + e^-$, respectively, which could be summarized as the total reaction of $1/2Zn + MnO_2 = Zn_{1/2}MnO_2$ in the full cell [36]. Figure 4a shows the cyclic voltammetry (CV) curves for the first cycle of Zn||MnO_2 and ZnO@Zn||MnO_2 cells measured at 0.1 mV s^{-1}. There are two pairs of redox peaks for both cells, which are ascribed to multistep redox processes of Mn^{4+}/Mn^{3+} [18]. The ZnO@Zn||MnO_2 cell displays enhanced current density and smaller potential difference than those of the Zn||MnO_2, demonstrating its lower polarization.

Figure 4b compares the first charge–discharge profiles of Zn||MnO_2 and ZnO@Zn||MnO_2 cells at 0.1C (1C = 308 mAh g^{-1}). The ZnO@Zn||MnO_2 cell exhibited a high discharging specific capacity of about 296.2 mAh g^{-1}. The Zn||MnO_2 cell showed similar discharge/charge behavior to that of ZnO@Zn||MnO_2, but with a lower specific capacity of 282.2 mAh g^{-1}. Figures S8 and S9 show the long-term cycling performance at 2C of ZnO@Zn-30||MnO_2 and ZnO@Zn-70||MnO_2, respectively, demonstrating worse cycling stabilities than that of ZnO@Zn||MnO_2. The excellent cycling performance is ascribed to the dense textured ZnO layer, which leads to the reduction of electrode corrosion as well as the generation of by-products, which is consistent with the FESEM

results in Figures S2 and S3. Figure 4c compares the rate performance of Zn||MnO_2 and ZnO@Zn||MnO_2 cells. The ZnO@Zn||MnO_2 cell showed improved rate performance compared to the Zn||MnO_2 cell with specific capacities of 296.2, 250.1, 210.9, 185.4, 158.6 and 114.4 mAh g^{-1} at 0.1, 0.2, 0.5, 1, 2 and 5C, respectively.

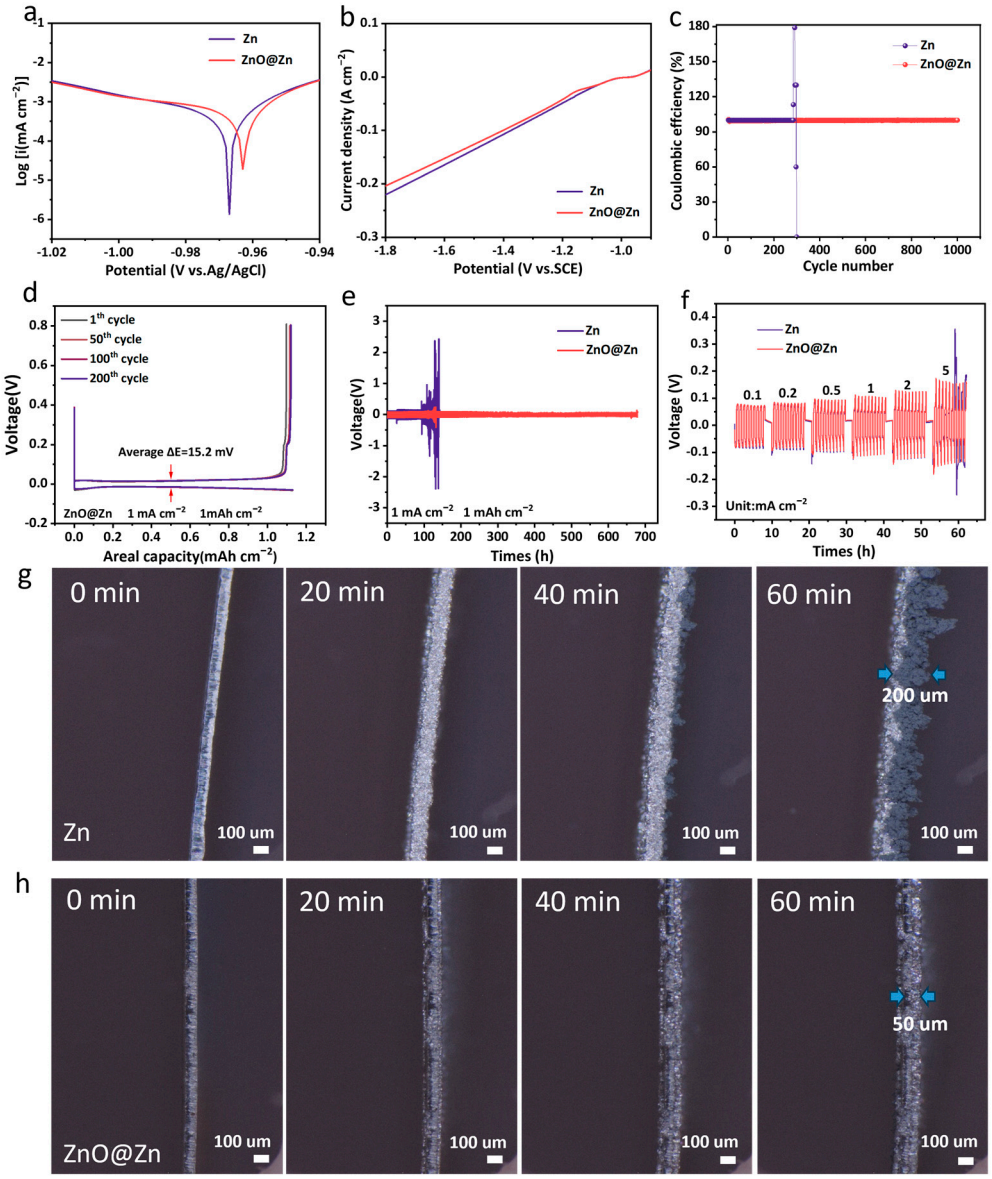

Figure 3. (**a**) Tafel corrosion curves and (**b**) linear sweep voltammetry (LSV) curves of bare Zn and ZnO@Zn in a three-electrodes system. (**c**) Coulombic efficiencies and (**d**) corresponding voltage curves at different cycles in the Zn||Cu and ZnO@Zn||Cu cells. (**e**) Long-term stability 1 mA cm^{-2}/1 mAh cm^{-2} and (**f**) rate performance at different current densities in the Zn||Zn and ZnO@Zn||ZnO@Zn symmetric cells. In situ optical observation of the Zn deposition on (**g**) bare Zn and (**h**) ZnO@Zn at a current density of 10 mA cm^{-2} for 60 min.

Figure 4d compares the long cycling performance of Zn||MnO_2 and ZnO@Zn||MnO_2 cells at 2C. Notably, ZnO@Zn||MnO_2 exhibited excellent stability against cycling with almost no capacity fading after 1100 cycles, far beyond that of the Zn||MnO_2 cell. The coated ZnO layers can effectively reduce the contact of electrode and electrolyte, minimize the occurrence of HERs and increase the reversibility of Zn^{2+}/Zn stripping/plating [9,17], which enhance the cycling stability of the ZnO@Zn||MnO_2 cell. The phenomenon of capacity growth during cycling is due to the participation of manganese ions in the electrolyte

in the charging process, leading to the generation of additional active materials through electrodeposition [37].

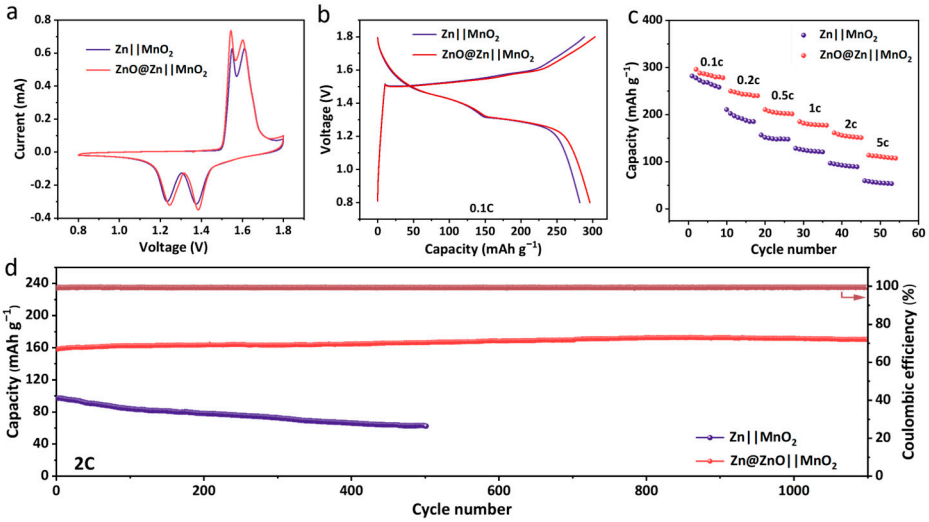

Figure 4. Electrochemical performance of full cells using MnO_2 as cathode. (**a**) CV curves at a scan rate of 0.1 mV s^{-1}. (**b**) Galvanostatic charge–discharge profiles at 0.1C. (**c**) Rate performance. (**d**) Long-term cycling performance.

To reveal the situation of Zn dendritic growth, the surface morphologies of bare Zn and ZnO@Zn in full cells after 400 cycles at 2C were obtained by FE-SEM measurements. As shown in Figure 5a,b, the bare Zn surface clearly exhibited an uneven deposition layer with sheet-like Zn dendritic growth, inducing low redox kinetics and poor cycling stability. In contrast, the deposited layer on the ZnO@Zn surface was more uniform (Figure 5c,d), which effectively improved the cycling stability of the ZnO@Zn||MnO_2 cell. Figures 5e and S10 show the XRD patterns of bare Zn and ZnO@Zn in full cells after 400 cycles. The bare Zn exhibited more obvious peaks of ZSH by-products than the ZnO@Zn, revealing its active interfacial reaction and corrosion on the surface. The ZnO@Zn exhibited a higher intensity ratio of $I_{(002)}/I_{(101)}$ (0.66) than that of bare Zn (0.58), demonstrating the enhanced (002) texture. Figure S11 shows the XPS survey spectrum of bare Zn and ZnO@Zn after 400 cycles. Both electrodes exhibited S elements after cycles, which were ascribed to the ZSH by-products. However, the content of S in the ZnO@Zn (Table S1 in Supplementary Materials) was much lower than that of bare Zn, indicating the lower formation of ZSH. Figure 5f shows the high-resolution S2p XPS spectrum of bare Zn and ZnO@Zn after 400 cycles. There were two characteristic peaks at 170.5 and 169.3 eV, corresponding to $S2p_{1/2}$ and $S2p_{3/2}$ [38]. The ZnO@Zn exhibited lower intensity than that of bare Zn, demonstrating the lower formation of sulfates, which was consistent with the XRD results.

To reveal the influence of ZnO coating on Zn^{2+}/Zn stripping/plating, DFT calculations using the Vienna Abinitio Simulation Package (VASP) were performed. A theoretical framework was devised to compute the adsorption energies on both (002) and (101) planes (Figure 5g) [22,39]. For a pristine Zn anode, the adsorption energy on the (002) plane significantly surpassed that of the (101) plane, suggesting a preferential deposition of zinc ions on the (101) surface (Figure S12) [14]. This preferential deposition was a primary contributor to the non-uniform deposition of Zn^{2+}. In contrast, after the coating of the ZnO layer, the (101) plane showed higher adsorption energy, which effectively inhibited Zn^{2+} deposition (Figure 5h). The lower adsorption energy of the (002) plane facilitates the deposition of Zn^{2+} on its surface, which facilitates lower Zn dendritic growth.

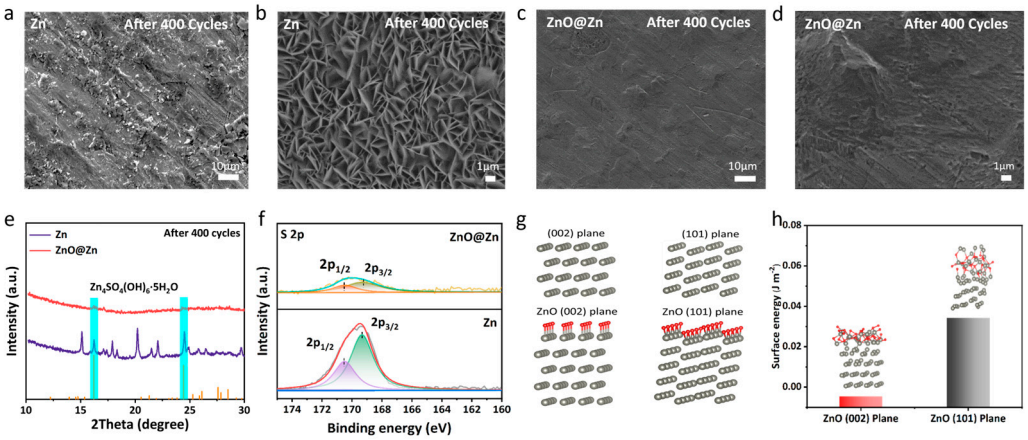

Figure 5. FE-SEM images of bare Zn (**a**,**b**) and ZnO@Zn (**c**,**d**) in full cells after 400 cycles at 2C. (**e**) XRD patterns and (**f**) high-resolution S 2p XPS spectrum of bare Zn and ZnO@Zn after 400 cycles. (**g**) Calculation models of theoretical computation. (**h**) Free energies of Zn atoms adsorbed on (002) and (101) planes of bare Zn and ZnO@Zn.

4. Conclusions

A ZnO-coated Zn anode (ZnO@Zn) for long-term aqueous zinc metal batteries (AZMBs) was designed by a facile and rapid approach using the ALD technique. The ZnO@Zn anode exhibits high stability with almost no capacity decay after 1100 cycles at 2C in a full cell using MnO_2 as the cathode. The ZnO layer can effectively lower the adsorption energy of the Zn(002) plane in ZnO@Zn, inducing the preferential deposition of Zn towards the (002) crystal plane. What is more, the ZnO coating is conducive to reducing corrosion and the generation of by-products, thus increasing the reversibility of Zn^{2+}/Zn stripping/plating. The ZnO@Zn material reported in this paper holds great promise for fabricating highly stable AZMBs.

Supplementary Materials: The following supporting information can be downloaded at: https://www.mdpi.com/article/10.3390/batteries10060178/s1, Figure S1: Raman spectra of bare Zn and ZnO@Zn; Figure S2: SEM image of ZnO@Zn-30; Figure S3: SEM image of ZnO@Zn-70; Figure S4: Cross-sectional image of ZnO@Zn; Figure S5: TEM image of ZnO on ZnO@Zn; Figure S6: Galvanostatic cycling curves of Zn||Cu half cell; Figure S7: Comparison of average voltage hysteresis of ZnO@Zn in this work with the reported modified Zn anode in literature [40–48]; Figure S8: Long-term cycling performance of ZnO@Zn-30 at 2C; Figure S9: Long-term cycling performance of ZnO@Zn-70 at 2C; Figure S10: XRD patterns of bare Zn and ZnO@Zn after 400 cycles; Figure S11: XPS survey spectrum of bare Zn and ZnO@Zn after 400 cycles; Figure S12: Adsorption energy of bare Zn on different planes; Table S1: The proportion of element content of bare Zn and ZnO@Zn after 400 cycles.

Author Contributions: Conceptualization, H.Z. and C.W.; methodology, H.Z. and F.L.; software, L.G. and F.L.; validation, H.Z., F.L. and Z.L.; formal analysis, H.Z.; investigation, B.X.; resources, C.W.; data curation, H.Z.; writing—original draft preparation, H.Z.; writing—review and editing, B.X. and C.W.; visualization, H.Z.; supervision, C.W.; project administration, C.W.; funding acquisition, C.W. Both H.Z. and F.L. contributed equally to this work and should be considered co-first authors. All authors have read and agreed to the published version of the manuscript.

Funding: This research was funded by the Natural Science Foundation of Shandong Province (No. ZR2022QB025).

Data Availability Statement: The data are available upon request from the corresponding authors.

Conflicts of Interest: The authors declare no competing financial interest.

References

1. Li, H.; Guo, S.; Zhou, H. Recent Advances in Manipulating Strategy of Aqueous Electrolytes for Zn Anode Stabilization. *Energy Storage Mater.* **2023**, *56*, 227–257. [CrossRef]
2. Bai, L.; Hu, Z.; Hu, C.; Zhang, S.; Ying, Y.; Zhang, Y.; Li, L.; Zhang, H.; Li, N.; Shi, S.; et al. Utilizing Cationic Vacancies and Spontaneous Polarization on Cathode to Enhance Zinc-Ion Storage and Inhibit Dendrite Growth in Zinc-Ion Batteries. *Angew. Chemie-Int. Ed.* **2023**, *62*, 2301631. [CrossRef] [PubMed]
3. He, P.; Huang, J. Chemical Passivation Stabilizes Zn Anode. *Adv. Mater.* **2022**, *34*, 2109872. [CrossRef] [PubMed]
4. Ma, L.; Li, N.; Long, C.; Dong, B.; Fang, D.; Liu, Z.; Zhao, Y.; Li, X.; Fan, J.; Chen, S.; et al. Achieving Both High Voltage and High Capacity in Aqueous Zinc-Ion Battery for Record High Energy Density. *Adv. Funct. Mater.* **2019**, *29*, 1906142. [CrossRef]
5. Yang, J.; Zhao, R.; Wang, Y.; Hu, Z.; Wang, Y.; Zhang, A.; Wu, C.; Bai, Y. Insights on Artificial Interphases of Zn and Electrolyte: Protection Mechanisms, Constructing Techniques, Applicability, and Prospective. *Adv. Funct. Mater.* **2023**, *33*, 2213510. [CrossRef]
6. Liu, C.; Li, Z.; Zhang, X.; Xu, W.; Chen, W.; Zhao, K.; Wang, Y.; Hong, S.; Wu, Q.; Li, M.C.; et al. Synergic Effect of Dendrite-Free and Zinc Gating in Lignin-Containing Cellulose Nanofibers-MXene Layer Enabling Long-Cycle-Life Zinc Metal Batteries. *Adv. Sci.* **2022**, *9*, 2202380. [CrossRef]
7. Shen, Q.; Wang, Y.; Han, G.; Li, X.; Yuan, T.; Sun, H.; Gong, Y.; Chen, T. Recent Progress in Electrolyte Additives for Highly Reversible Zinc Anodes in Aqueous Zinc Batteries. *Batteries* **2023**, *9*, 284. [CrossRef]
8. Zhou, Y.; Xie, S.; Li, Y.; Zheng, Z.; Dong, L. Sieve-Like Interface Built by ZnO Porous Sheets towards Stable Zinc Anodes. *J. Colloid Interface Sci.* **2023**, *630*, 676–684. [CrossRef] [PubMed]
9. Lu, H.; Jin, Q.; Jiang, X.; Dang, Z.M.; Zhang, D.; Jin, Y. Vertical Crystal Plane Matching between $AgZn_3$ (002) and Zn(002) Achieving a Dendrite-Free Zinc Anode. *Small* **2022**, *18*, 2200131. [CrossRef]
10. Zhang, H.; Zhong, Y.; Li, J.; Liao, Y.; Zeng, J.; Shen, Y.; Yuan, L.; Li, Z.; Huang, Y. Inducing the Preferential Growth of Zn(002) Plane for Long Cycle Aqueous Zn-Ion Batteries. *Adv. Energy Mater.* **2023**, *13*, 2203254. [CrossRef]
11. Shangguan, M.; Wang, K.; Zhao, Y.; Xia, L. Tetraethylene Glycol Dimethyl Ether (TEGDME)-Water Hybrid Electrolytes Enable Excellent Cyclability in Aqueous Zn-Ion Batteries. *Batteries* **2023**, *9*, 462. [CrossRef]
12. Kong, D.; Zhang, Q.; Li, L.; Zhao, H.; Liu, R.; Guo, Z.; Wang, L. A Self-Growing 3D Porous Sn Protective Layer Enhanced Zn Anode. *Batteries* **2023**, *9*, 262. [CrossRef]
13. Yang, H.; Chang, Z.; Qiao, Y.; Deng, H.; Mu, X.; He, P.; Zhou, H. Constructing a Super-Saturated Electrolyte Front Surface for Stable Rechargeable Aqueous Zinc Batteries. *Angew. Chemie* **2020**, *132*, 9463–9467. [CrossRef]
14. Zhao, Z.; Wang, R.; Peng, C.; Chen, W.; Wu, T.; Hu, B.; Weng, W.; Yao, Y.; Zeng, J.; Chen, Z.; et al. Horizontally Arranged Zinc Platelet Electrodeposits Modulated by Fluorinated Covalent Organic Framework Film for High-Rate and Durable Aqueous Zinc Ion Batteries. *Nat. Commun.* **2021**, *12*, 6606. [CrossRef] [PubMed]
15. Peng, H.; Wang, X.; Liu, Z.; Lei, H.; Cui, S.; Xie, X.; Hu, Y.; Ma, G. Alleviating Zn Dendrites by Growth of Ultrafine ZnO Nanowire Arrays through Horizontal Anodizing for High-Capacity, Long-Life Zn Ion Capacitors. *ACS Appl. Mater. Interfaces* **2023**, *15*, 4071–4080. [CrossRef] [PubMed]
16. Wang, H.; Chen, Y.; Yu, H.; Liu, W.; Kuang, G.; Mei, L.; Wu, Z.; Wei, W.; Ji, X.; Qu, B.; et al. A Multifunctional Artificial Interphase with Fluorine-Doped Amorphous Carbon Layer for Ultra-Stable Zn Anode. *Adv. Funct. Mater.* **2022**, *32*, 2205600. [CrossRef]
17. Feng, J.; Li, X.; Cui, X.; Zhao, H.; Xi, K.; Ding, S. Periodically Alternating Electric Field Layers Induces the Preferential Growth of Zn(002) Plane for Ultralow Overpotential Zinc-Ion Batteries. *Adv. Energy Mater.* **2023**, *13*, 2204092. [CrossRef]
18. Chen, M.; Yang, M.; Zhou, W.; Tian, Q.; Han, X.; Chen, J.; Zhang, P. Oriented Zn Plating Guided by Aligned ZnO Hexagonal Columns Realizing Dendrite-Free Zn Metal Electrodes. *J. Colloid Interface Sci.* **2023**, *644*, 368–377. [CrossRef]
19. Xin, T.; Wang, Y.; Xu, Q.; Shang, J.; Yuan, X.; Song, W.; Liu, J. Forming an Amorphous ZnO Nanosheet Network by Confined Parasitic Reaction for Stabilizing Zn Anodes and Reducing Water Activity. *ACS Appl. Energy Mater.* **2022**, *5*, 2290–2299. [CrossRef]
20. Hu, X.; Borowiec, J.; Zhu, Y.; Liu, X.; Wu, R.; Ganose, A.M.; Parkin, I.P.; Boruah, B.D. Dendrite-Free Zinc Anodes Enabled by Exploring Polar-Face-Rich 2D ZnO Interfacial Layers for Rechargeable Zn-Ion Batteries. *Small* **2023**, *2306827*, 2306827. [CrossRef]
21. Liu, Y.; Chen, S.; Yuan, H.; Xiong, F.; Liu, Q.; An, Y.; Zhang, J.; Wu, L.; Sun, J.; Zhang, Y.W.; et al. Achieving Highly Reversible Zinc Metal Anode via Surface Termination Chemistry. *Sci. Bull.* **2023**, *68*, 2993–3002. [CrossRef]
22. Wang, R.; Xin, S.; Chao, D.; Liu, Z.; Wan, J.; Xiong, P.; Luo, Q.; Hua, K.; Hao, J.; Zhang, C. Fast and Regulated Zinc Deposition in a Semiconductor Substrate toward High-Performance Aqueous Rechargeable Batteries. *Adv. Funct. Mater.* **2022**, *32*, 2207751. [CrossRef]
23. Wei, T.; Zhang, H.; Ren, Y.; Mo, L.; He, Y.; Tan, P.; Huang, Y.; Li, Z.; Zhu, D.; Hu, L. Building Near-Unity Stacked (002) Texture for High-Stable Zinc Anode. *Adv. Funct. Mater.* **2023**, *34*, 2312506. [CrossRef]
24. Zhang, Y.; Han, X.; Liu, R.; Yang, Z.; Zhang, S.; Zhang, Y.; Wang, H.; Cao, Y.; Chen, A.; Sun, J. Manipulating the Zinc Deposition Behavior in Hexagonal Patterns at the Preferential Zn (100) Crystal Plane to Construct Surficial Dendrite-Free Zinc Metal Anode. *Small* **2022**, *18*, 2105978. [CrossRef]
25. Li, T.; Hu, S.; Wang, C.; Wang, D.; Xu, M.; Chang, C.; Xu, X.; Han, C. Engineering Fluorine-Rich Double Protective Layer on Zn Anode for Highly Reversible Aqueous Zinc-Ion Batteries. *Angew. Chemie Int. Ed.* **2023**, *62*, 2314883. [CrossRef] [PubMed]
26. Deng, D.; Fu, K.; Yu, R.; Zhu, J.; Cai, H.; Zhang, X.; Wu, J.; Luo, W.; Mai, L. Ion Tunnel Matrix Initiated Oriented Attachment for Highly Utilized Zn Anodes. *Adv. Mater.* **2023**, *35*, 2302353. [CrossRef]

27. Jia, R.; Zhang, R.; Yu, L.; Kong, X.; Bao, S.; Tu, M.; Liu, X.; Xu, B. Engineering a Hierarchical Carbon Supported Magnetite Nanoparticles Composite from Metal Organic Framework and Graphene Oxide for Lithium-Ion Storage. *J. Colloid Interface Sci.* **2023**, *630*, 86–98. [CrossRef] [PubMed]
28. Blöchl, P.E. Projector Augmented-Wave Method. *Phys. Rev. B* **1994**, *50*, 17953–17979. [CrossRef]
29. Allouche, A. Software News and Updates Gabedit—A Graphical User Interface for Computational Chemistry Softwares. *J. Comput. Chem.* **2012**, *32*, 174–182. [CrossRef]
30. Yang, H.G.; Sun, C.H.; Qiao, S.Z.; Zou, J.; Liu, G.; Smith, S.C.; Cheng, H.M.; Lu, G.Q. Anatase TiO_2 Single Crystals with a Large Percentage of Reactive Facets. *Nature* **2008**, *453*, 638–641. [CrossRef]
31. Yin, H.; Liu, Y.; Zhu, Y.; Ye, F.; Xu, G.; Lin, M.; Kang, W. Bimetal-Initiated Concerted Zn Regulation Enabling Highly Stable Aqueous Zn-Ion Batteries. *Batteries* **2024**, *10*, 70. [CrossRef]
32. Kim, E.; Vaynzof, Y.; Sepe, A.; Guldin, S.; Scherer, M.; Cunha, P.; Roth, S.V.; Steiner, U. Gyroid-Structured 3D ZnO Networks Made by Atomic Layer Deposition. *Adv. Funct. Mater.* **2014**, *24*, 863–872. [CrossRef]
33. Fan, C.; Meng, W.; Li, D.; Jiang, L. Stratified Adsorption Strategy Facilitates Highly Stable Dendrite Free Zinc Metal Anode. *Energy Storage Mater.* **2023**, *56*, 468–477. [CrossRef]
34. Han, Y.; Wang, F.; Zhang, B.; Yan, L.; Hao, J.; Zhu, C.; Zou, X.; Zhou, Y.; Xiang, B. Building Block Effect Induces Horizontally Oriented Bottom Zn(002) Deposition for a Highly Stable Zinc Anode. *Energy Storage Mater.* **2023**, *62*, 102928. [CrossRef]
35. Bao, S.; Tu, M.; Huang, H.; Wang, C.; Chen, Y.; Sun, B.; Xu, B. Heterogeneous Iron Oxide Nanoparticles Anchored on Carbon Nanotubes for High-Performance Lithium-Ion Storage and Fenton-like Oxidation. *J. Colloid Interface Sci.* **2021**, *601*, 283–293. [CrossRef]
36. Ke, X.; Li, L.; Wang, S.; Wang, A.; Jiang, Z.; Wang, F.R.; Kuai, C.; Guo, Y. Mn-Oxide Cathode Material for Aqueous Zn-Ion Battery: Structure, Mechanism, and Performance. *Next Energy* **2024**, *2*, 100095. [CrossRef]
37. Liang, R.; Fu, J.; Deng, Y.P.; Pei, Y.; Zhang, M.; Yu, A.; Chen, Z. Parasitic Electrodeposition in Zn-MnO_2 Batteries and Its Suppression for Prolonged Cyclability. *Energy Storage Mater.* **2021**, *36*, 478–484. [CrossRef]
38. Xie, F.; Li, H.; Wang, X.; Zhi, X.; Chao, D.; Davey, K.; Qiao, S.Z. Mechanism for Zincophilic Sites on Zinc-Metal Anode Hosts in Aqueous Batteries. *Adv. Energy Mater.* **2021**, *11*, 2003419. [CrossRef]
39. Zhao, R.; Dong, X.; Liang, P.; Li, H.; Zhang, T.; Zhou, W.; Wang, B.; Yang, Z.; Wang, X.; Wang, L.; et al. Prioritizing Hetero-Metallic Interfaces via Thermodynamics Inertia and Kinetics Zincophilia Metrics for Tough Zn-Based Aqueous Batteries. *Adv. Mater.* **2023**, *35*, 2209288. [CrossRef]
40. Li, Y.; Jia, H.; Ali, U.; Liu, B.; Gao, Y.; Li, L.; Zhang, L.; Chai, F.; Wang, C. In-Situ Interfacial Layer with Ultrafine Structure Enabling Zinc Metal Anodes at High Areal Capacity. *Chem. Eng. J.* **2022**, *450*, 138374. [CrossRef]
41. Tan, L.; Wei, C.; Zhang, Y.; An, Y.; Xiong, S.; Feng, J. Long-Life and Dendrite-Free Zinc Metal Anode Enabled by a Flexible, Green and Self-Assembled Zincophilic Biomass Engineered MXene Based Interface. *Chem. Eng. J.* **2022**, *431*, 134277. [CrossRef]
42. Wang, M.; Wu, X.; Yang, D.; Zhao, H.; He, L.; Su, J.; Zhang, X.; Yin, X.; Zhao, K.; Wang, Y.; et al. A Colloidal Aqueous Electrolyte Modulated by Oleic Acid for Durable Zinc Metal Anode. *Chem. Eng. J.* **2023**, *451*, 138589. [CrossRef]
43. Li, Y.; Wu, P.; Zhong, W.; Xie, C.; Xie, Y.; Zhang, Q.; Sun, D.; Tang, Y.; Wang, H. A Progressive Nucleation Mechanism Enables Stable Zinc Stripping-Plating Behavior. *Energy Environ. Sci.* **2021**, *14*, 5563–5571. [CrossRef]
44. Qin, H.; Kuang, W.; Hu, N.; Zhong, X.; Huang, D.; Shen, F.; Wei, Z.; Huang, Y.; Xu, J.; He, H. Building Metal-Molecule Interface towards Stable and Reversible Zn Metal Anodes for Aqueous Rechargeable Zinc Batteries. *Adv. Funct. Mater.* **2022**, *32*, 2206695. [CrossRef]
45. Li, Y.; Jia, H.; Ali, U.; Wang, H.; Liu, B.; Li, L.; Zhang, L.; Wang, C. Successive Gradient Internal Electric Field Strategy Toward Dendrite-Free Zinc Metal Anode. *Adv. Energy Mater.* **2023**, *13*, 2301643. [CrossRef]
46. Wang, Y.; Guo, T.; Yin, J.; Tian, Z.; Ma, Y.; Liu, Z.; Zhu, Y.; Alshareef, H.N. Controlled Deposition of Zinc-Metal Anodes via Selectively Polarized Ferroelectric Polymers. *Adv. Mater.* **2022**, *34*, 2106937. [CrossRef]
47. Liu, H.; Wang, J.G.; Hua, W.; Sun, H.; Huyan, Y.; Tian, S.; Hou, Z.; Yang, J.; Wei, C.; Kang, F. Building Ohmic Contact Interfaces toward Ultrastable Zn Metal Anodes. *Adv. Sci.* **2021**, *8*, 2102612. [CrossRef]
48. Liu, Z.; Li, G.; Xi, M.; Huang, Y.; Li, H.; Jin, H.; Ding, J.; Zhang, S.; Zhang, C.; Guo, Z. Interfacial Engineering of Zn Metal via a Localized Conjugated Layer for Highly Reversible Aqueous Zinc Ion Battery. *Angew. Chemie Int. Ed.* **2024**, *63*, 2319091.